2-1-2022

The Role of Slow Slip Events in the Cascadia Subduction Zone Earthquake Cycle

Juliette P. Saux
Smith College

Elias G. Molitors Bergman
Smith College

Eileen L. Evans
California State University, Northridge

John P. Loveless
Smith College, jloveles@smith.edu

Recommended Citation

JGR Solid Earth

The Role of Slow Slip Events in the Cascadia Subduction Zone Earthquake Cycle

Juliette P. Saux[1] , **Elias G. Molitors Bergman[1]** , **Eileen L. Evans[2]** , and **John P. Loveless[1]**

[1]Department of Geosciences, Smith College, Northampton, MA, USA, [2]Department of Geological Sciences, California State University-Northridge, Northridge, CA, USA

Abstract Slow slip events (SSEs) detected on the Cascadia Subduction Zone interface at 30–50 km depth imply a release of accumulated strain. However, studies of interseismic deformation in Cascadia typically find coupling on the upper 30 km of the interface, which is generally accepted as defining the seismogenic zone. Estimates of coupling using net interseismic velocities (including SSE effects) and restricting coupling to the shallow interface may underestimate slip deficit accumulation at depths >30 km. Here, we detect reversals in GPS motion as indications of SSEs, then use SSE displacements to estimate cumulative slow slip from 2007 to 2021. We calculate pure interseismic velocities, correcting for SSE displacements, and use them to constrain an elastic block model, estimating slip deficit on the subduction interface down to 50 km. By evaluating slip deficit and slow slip independently, we examine SSEs' effect on interseismic strain accumulation, and the effect of inter-SSE slip deficit and slow slip on vertical deformation of the forearc. We find that moderate to high coupling extends to 40 km depth, and while shallow coupling is consistent with previous estimates of the seismogenic zone, a deeper region of slip deficit beneath the Olympic Peninsula may be partially (61%) relieved aseismically by SSEs. Patterns of surface uplift suggest that complete relief of deep coupling over multiple decades may be accomplished by time-varying rates of aseismic slip.

Plain Language Summary Subduction zones, where tectonic plates converge, are responsible for the world's largest earthquakes and present significant seismic risk to the surrounding regions. The Cascadia Subduction Zone, which extends from northern California to Vancouver Island, has not produced a great earthquake since 1700, suggesting that strain has been accumulating for over 300 years. Previous studies suggest that the shallow (<30 km depth) portion of the fault has been coupled, allowing strain to accumulate, and slow slip events (SSEs), a form of slow strain release that does not produce the shaking that typically occurs during an earthquake, have been detected on the fault at greater depths. Here, we test the assumption that fault coupling is restricted to the shallow portion of the fault interface and examine the role that SSEs play in the strain accumulation and release cycle. Because the magnitude of great earthquakes is related to the area of the fault that ruptures, gaining a better understanding of the interaction between SSEs and coupling is crucial to understanding the seismic hazard posed by the Cascadia Subduction Zone.

1. Introduction

The Cascadia Subduction Zone, where the Juan de Fuca plate moves northeastward relative to stable North America and subducts under the North American plate at a rate of ~40 mm/year (Figure 1; DeMets et al., 2010; Wang & Tréhu, 2016), has the ability to produce great megathrust earthquakes ($M_w \geq 8.0$; Atwater, 1987; Goldfinger et al., 2003). A lack of macroseismicity in the region for the past 300 years, as well as GPS observations from the Pacific Northwest that show northeastward motion of the North American plate, suggests that the overriding North American plate is frictionally locked to the subducting oceanic plate, causing stress to accumulate on the fault (Almeida et al., 2018; Hyndman & Wang, 1993; Krogstad et al., 2016; Schmalzle et al., 2014).

Knowing the spatial extent of the zone of locking on the subduction interface is critical to understanding the potential seismic hazard posed by the fault (Loveless & Meade, 2011; Moreno et al., 2010; Protti et al., 2014). Using interseismic GPS observations, we can estimate the degree of coupling on the subduction interface. Here, coupling is defined as the ratio of the interseismic slip deficit rate to the plate convergence rate (Bürgmann, 2018) and therefore gives a kinematic description of fault behavior. We adopt the definitions of coupling and locking used from Herman et al. (2018): areas of the fault that are frictionally locked are, by definition, also coupled, whereas not all portions that are coupled are locked; the portions of the interface adjacent to a locked asperity
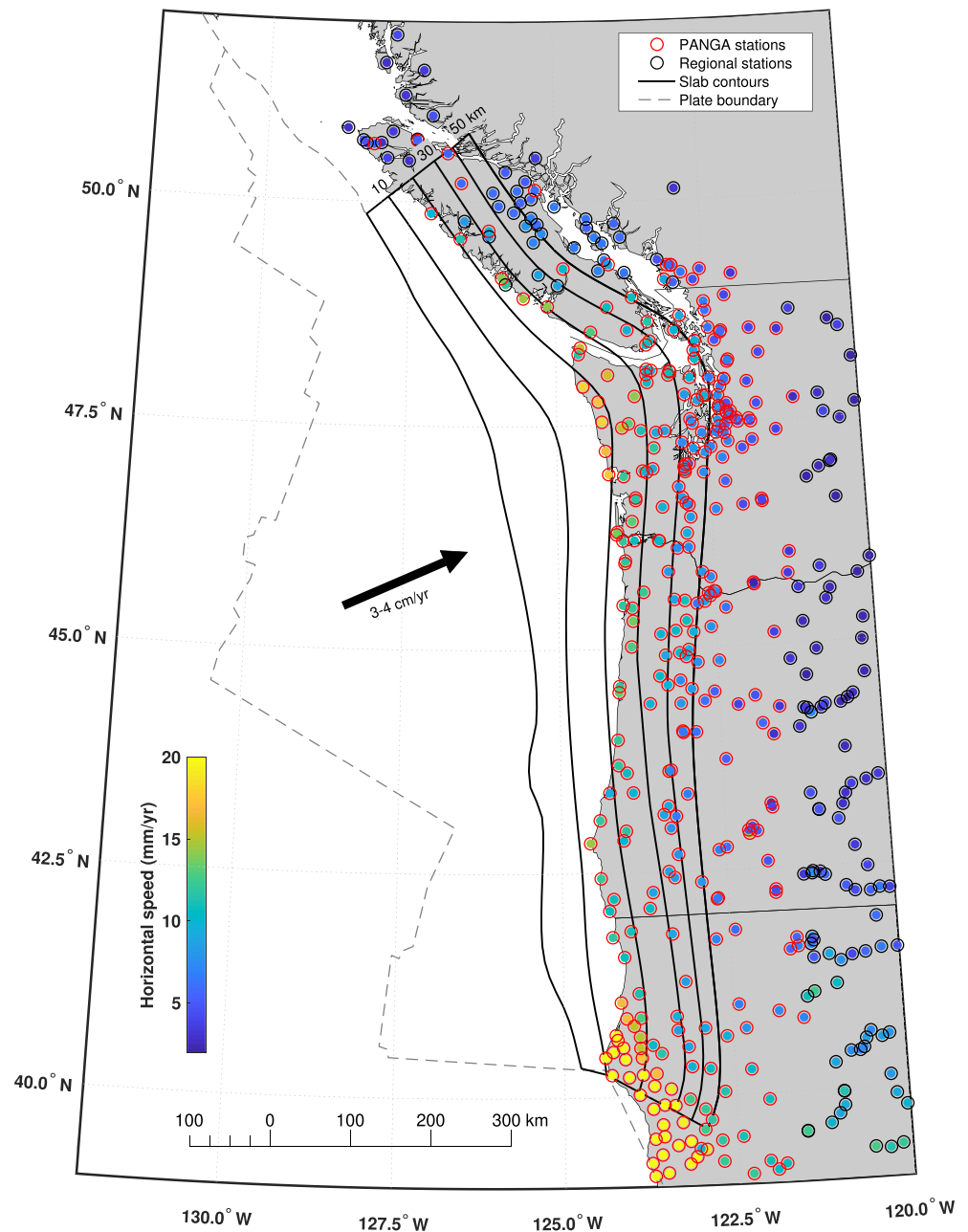
Figure 1. Map of net interseismic speed of geodetic stations, expressed relative to North America, from the Pacific Northwest Geodetic Array (PANGA; red outlines) and stations from a regional velocity field (black outlines; McCaffrey et al., 2013). Black lines show 10 km slab depth contours (McCrory et al., 2006) and gray lines show block model boundaries. Black arrow represents the approximate motion of the Juan de Fuca plate relative to stable North America (DeMets et al., 2010).

might not be frictionally stuck together but are still unable to fully slide past each other, resulting in a positive and nonzero coupling ratio. By examining coupling, we can make inferences about which zones are frictionally locked and, by extension, about the spatial extent of the potential seismogenic zone.

In Cascadia, where the subducting slab is young and warm, the seismogenic zone has been considered to be restricted to the upper 30 km of the subduction interface (between the 350°C and 450°C isotherms), where the fault could exhibit velocity weakening behavior (Gao & Wang, 2017; Hyndman & Wang, 1993; Oleskevich et al., 1999). Previous estimates of coupling based on interseismic GPS observations suggest that coupling is

restricted to the updip portion of the subduction interface, consistent with assumed location of the seismogenic zone (Michel et al., 2019; Schmalzle et al., 2014). Schmalzle et al. (2014) presented two models: one assuming a smooth bell-shaped distribution of coupling, with low coupling near the updip and downdip extents of the interface, and the other showing a gradual and linear decrease from full coupling at the trench to creep at around 30 km depth. Although estimates differ in whether the fault is coupled at the trench, most agree that coupling decreases with depth (Michel et al., 2019; Schmalzle et al., 2014). Viscoelastic models attribute motion far from the subduction trench (near the volcanic arc) to relaxation of the lower crust and upper mantle, while limiting coupling to the upper 20 km of the subduction interface, consistent with results from thermal modeling (Li et al., 2018; Pollitz & Evans, 2017). Other studies have tested elastic models of deformation due to interface slip that are time independent and require coupling to extend past the assumed downdip limit of the seismogenic zone to fit the same GPS data (Li et al., 2018; Wang & Tréhu, 2016).

Complicating geodetically informed estimates of interseismic coupling in Cascadia is the recurrence of slow slip events (SSEs), an aseismic slip process that has also been imaged on other fault systems around the globe, including the Nankai (Japan) and Guererro (Mexico) subduction zones (Nishimura et al., 2013; Radiguet et al., 2012) and the San Andreas fault (Rousset et al., 2019). Along the strike of the Cascadia Subduction Zone, SSEs have been detected in several distinct zones with recurrence intervals ranging from 12 to 23 months (Brudzinski & Allen, 2007) and are generally thought to occur around 30–50 km depth on the subduction interface (Gao & Wang, 2017; Michel et al., 2019; Szeliga et al., 2008), farther downdip than the expected zone of interseismic stress accumulation. SSEs have been recognized in geodetic time series as periodic reversals in the nominally interseismic trend, showing a westward component of motion lasting weeks to months (Dragert et al., 2001). Net interseismic velocities, which generally decay landward from the coastline (Figure 1), where the surface lies about 30–60 km above the subduction interface (Holtkamp & Brudzinski, 2010), differ from velocities between SSEs, which are faster inland than along the coastline. This discrepancy between net interseismic (including the impact of SSEs) and pure interseismic (inter-SSE) velocities calls into question the ability of the fault to be coupled deeper than 30 km depth and subsequently challenges previous estimates of the spatial distribution of coupling on the subduction interface. Holtkamp and Brudzinski (2010) explored the possibility of coupling at depths greater than 30 km using a 2-D representation of the plate interface, finding that some coupling is needed at depths up to 30 km to fit these pure interseismic velocities. Schmalzle et al. (2014) also used pure interseismic velocities to estimate coupling on the subduction interface but did not allow coupling to extend deeper than 30 km. Bartlow (2020) found that the cumulative slip pattern from SSEs is variable along the strike of the subduction zone, similar to previous observations of segmentation in SSE behavior from north to south (Brudzinski & Allen, 2007).

In this study, we evaluate whether SSEs release strain from coupling at depth, and therefore whether that deeper portion of the subduction interface can accumulate slip deficit over time, despite periodic slow slip. We use a slope-based detection algorithm to find reversals in motion in GPS data as indications of SSEs, then use SSE displacements to estimate the cumulative slow slip distribution. We correct GPS time series for the occurrence of SSEs in order to isolate pure interseismic velocities that characterize motion in between SSEs. We then compare the slow slip distribution to pure interseismic coupling from an elastic block model in order to understand the role of SSEs in balancing accumulated slip deficit. We test the previous assumption that coupling is confined to ≤30 km depth by estimating slip deficit on a three-dimensional representation of the subduction interface down to 50 km. Estimating pure interseismic slip deficit and slow slip separately allows us to compare individual slip processes on the subduction zone and assess the extent of the potential seismogenic zone.

2. Slow Slip Events

2.1. Geodetic Detection of Slow Slip Effects

SSEs in Cascadia have been interpreted from GPS time series that show a reversal in the nominally interseismic position change through time (e.g., Dragert et al., 2001). We developed a slope (velocity)-based algorithm to detect SSEs within geodetic daily position time series from 334 stations from the Pacific Northwest Geodetic Array (PANGA) spanning 1996–2021. This algorithm evaluates the long-term velocity over the time series duration, then uses a moving window to calculate average daily velocities. For each day, we calculate velocities as best fitting slopes across 3-week spans of daily position observations (corrected for step offsets from earthquakes and equipment maintenance and periodic signals representing seasonal impacts on position), first using
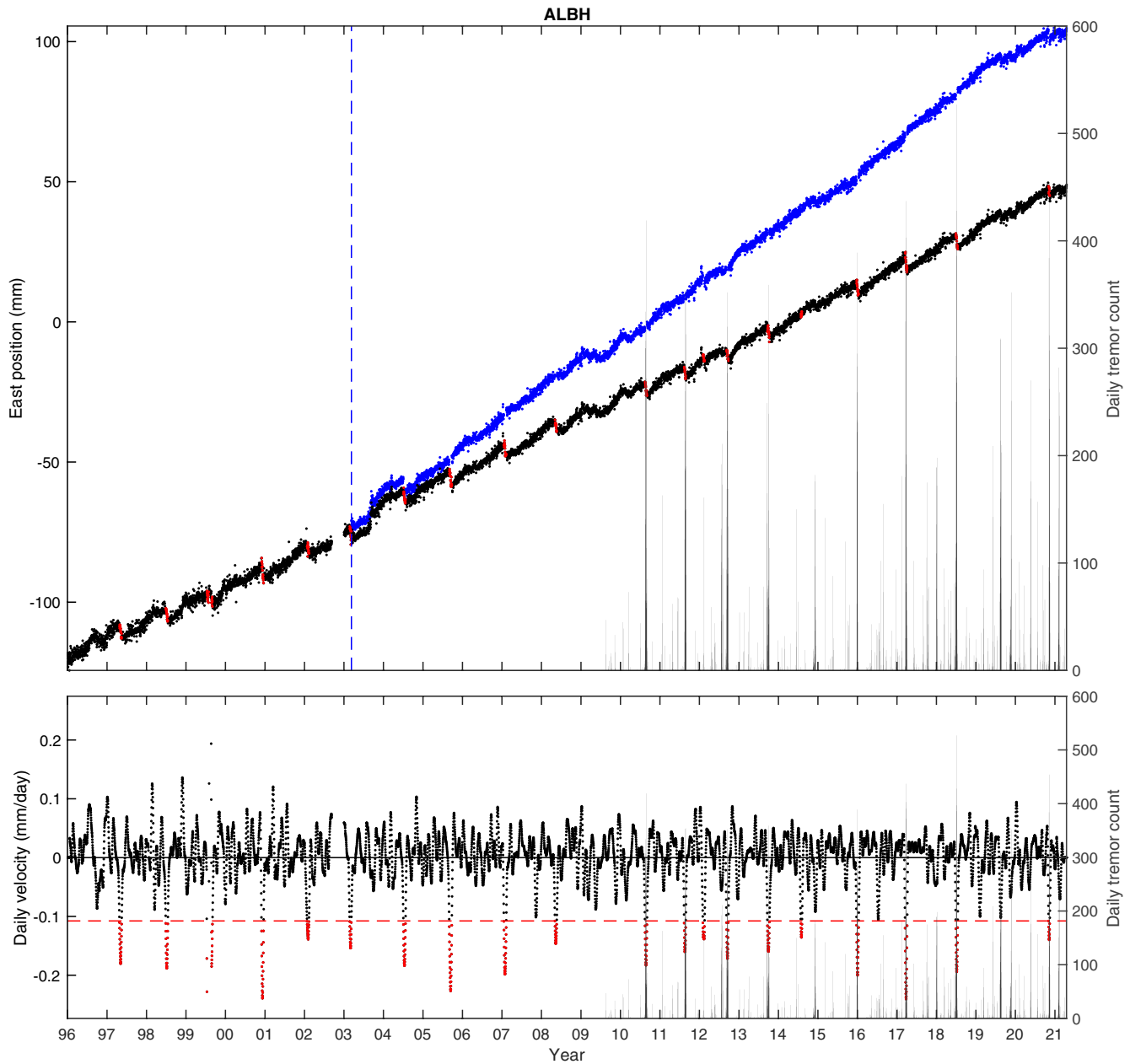
Figure 2. Example position time series and slow slip detection. Top: east position through time at station ALBH (−123.29°E, 48.23°N). Black points show raw east component position observations from Pacific Northwest Geodetic Array (PANGA), and overprinted red points show algorithmic detection of position reversals inferred to reflect slow slip. Blue points show pure interseismic deformation, calculated by removing slow slip reversals from events cataloged across the entire array after the date of the blue dashed vertical line. Bottom: daily velocities or scores, calculated as the average velocity from a 21-day moving window. We identify slow slip effects as daily velocities that are in the 90th percentile of the station's negative score (red points, below red dashed line). In both panels, vertical lines show daily tremor counts since 6 August 2009 (Pacific Northwest Seismic Network) for a 0.5° latitude range centered on the station's latitude. Time series plots for all PANGA stations used in this study can be found in the Supporting Information S1.

the target day as the last of the observations, then the second-to-last, etc. until the target day is the first of the daily positions used for the velocity calculation. We then average these 21 distinct window velocity estimates and identify target days for which the average daily velocity deviates from the long-term velocity, focusing on a westward component of motion that suggests reverse-sense slip on the underlying subduction zone (Dragert et al., 2001). These daily average velocities are used as a score (Figure 2, bottom), similar to that generated by Crowell et al. (2016), corresponding to the interpreted influence of an SSE on the station's motion on that day. We define an SSE detection on days for which the score is in the 90th percentile of the station's negative scores
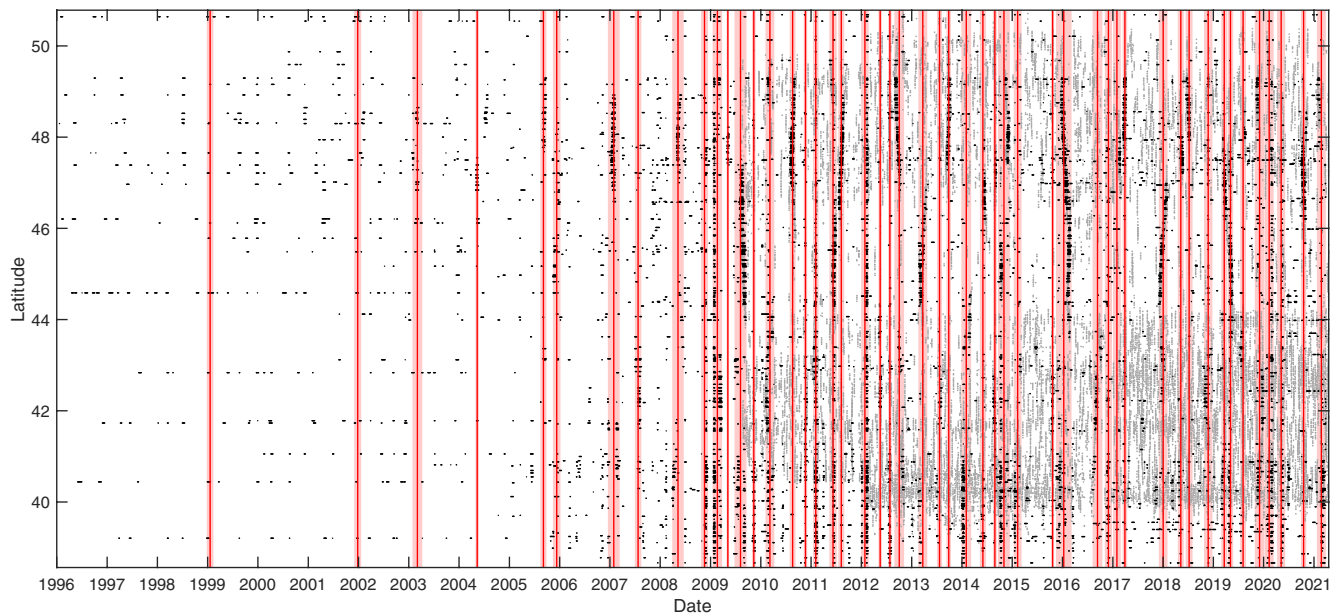
Figure 3. Catalog of geodetically detected slow slip events. Black points show daily detections at individual stations, which are compiled in time as cataloged events. Pink rectangles show the temporal extent of each cataloged event, while red lines mark event midpoints. The latitude span of the cataloged events is not meant to imply spatial continuity; black points that intersect each catalog event indicate the stations at which the event was detected. Gray dots indicate occurrence of tremor detected by the Pacific Northwest Seismic Network since 6 August 2009.

(corresponding to westward deviations in motion). The 3-week span used as a time window for averaging daily velocities at each station does not place bounds on the duration of SSEs, and the duration of the averaging window does not substantially impact the number or displacement field of detected events (Text S2 and Table S1 in Supporting Information S1). In general, detected reversals are temporally correlated with spikes in local tremor activity (Figures 2 and 3), consistent with previous work linking geodetic detection of SSEs with the occurrence of tremor (Bartlow, 2020; Dragert et al., 2004; Wech et al., 2009). Text S2 in Supporting Information S1 provides additional details about the detection algorithm and serves as a user's manual for our MATLAB codes (Loveless, Saux, et al., 2021).

2.2. Catalog of SSEs

After identifying reversals in individual station time series, we aggregate these detections in time to generate a catalog of SSEs. We define an event as consecutive days on which a reversal is detected at ≥10 stations, and the first and last day of detection across this subset of stations define the event duration. We detected reversals through each station's entire time series but focus on events since January 2007, detected at stations with greater spatial density across the entire Cascadia fore arc (Figure 3). We calculate displacement fields for each event by (a) linear least squares fitting of each station's position time series from the starting to ending day of its detection, (b) evaluating the function on the station's first and last detection days, and (c) taking the difference in these two positions. We define displacement uncertainties from the square root of the covariance of this least squares fit.

Because our focus is on the aggregate impact of SSEs on the earthquake cycle as observed by the geodetic network, we sum station displacements across all events to give a cumulative displacement field attributable to SSEs. As stations have been observing for varying time periods, we normalize each station's cumulative SSE displacement by its time series duration since 2007, framing the summed displacement as an average annual velocity. This yields an SSE velocity field with similar speeds at closely spaced stations, even if those stations have substantially different recording durations. We used the same summation and normalization approach to give cumulative uncertainties on the SSE velocities.

The resulting catalog contains 50 SSEs, 44 of which occurred after 2007 (Figure 3). We filtered out stations that were nearly collocated (choosing the station with the lowest estimated uncertainty of those within 0.5 km), those

at which no SSEs were detected, and those with outlier uncertainties (less than 0.02 mm/year or greater than 0.2 mm/year), yielding a cumulative SSE velocity field at 298 PANGA stations. Due to the nature of our temporal categorization of these events, some could be considered as distinct events, as detections are clustered in different latitudinal zones. Across the entire fore arc, we detect an SSE on average every 119 ± 60 days since 2007, though recurrence in a given location is longer and varies along strike (Brudzinski & Allen, 2007). Station ALBH on the Olympic Peninsula is well studied (Holtkamp & Brudzinski, 2010; Miller et al., 2002; Szeliga et al., 2008) and exhibits displacements from 11 cataloged SSEs at average intervals of 560 ± 212 days (Figure 2). Overall, we detect between 1 and 14 events at a given station. The catalog of SSEs detected using our velocity-based algorithm is broadly consistent with previous catalogs (Michel et al., 2019; Schmalzle et al., 2014; Szeliga et al., 2008) in terms of timing and displacements, and with the spatial and temporal distribution of nonvolcanic tremor detected since 2009 (Pacific Northwest Seismic Network; Figure 3). Across the network, cumulative SSE speeds average 2.1 mm/year (−2.0 mm/year in the east direction, −0.5 mm/year in the north direction), with a peak speed of 6.0 mm/year. Nominal uncertainties are small, averaging 0.08 mm/year, with a range of 0.02–0.2 mm/year. Using a lower percentile threshold and/or a longer daily velocity averaging span yields generally faster SSE velocities (Text S2, Table S1, and Figure S5 in Supporting Information S1).

2.3. Estimating Cumulative Slow Slip Distribution

From the cumulative velocity field determined from the detection algorithm, we estimate the distribution of slow slip rate on the subduction zone interface, which we represent using triangular dislocation elements (TDEs) that mimic the three-dimensional geometry proposed by McCrory et al. (2006). We calculate the partial derivatives relating unit slip rate on these elements to surface velocity at station coordinates (Meade, 2007) and then estimate the slow slip rate distribution for each event using Total Variation Regularization (TVR), which promotes a clustered slip distribution, minimizing unique magnitudes of slip rate across the entire model geometry (Chambolle, 2004; Evans et al., 2015; Grant & Boyd, 2008, 2014; Rudin et al., 1992). We use this regularization method to explore how distinct the spatial zonation of interseismic coupling and slow slip are, whereas using an alternative Laplacian smoothing method (Desbrun et al., 1999; Harris & Segall, 1987) to regularize the estimation could blur together regions that feature different slip styles.

TVR requires selection of a weighting factor, λ, that balances fit to the constraining geodetic data and regularization criteria. We test a range of λ, the lowest yielding a noisy slip rate distribution that almost perfectly fits SSE velocities, and the largest giving a poorer fit to velocities and homogeneous slip rate distribution across the entire subduction zone (except for narrow zones at the updip and downdip edge, where we have enforced zero slip in the estimation; Text S3 in Supporting Information S1). We do not constrain the elements' sense of strike slip, but because the SSE detection algorithm identifies westward motion as an indicator of slow slip, we force the sense of dip slip to be reverse. In general, residual station velocity magnitude increases and the number of unique slip rate values (i.e., model complexity) decreases as the regularization criteria are more heavily weighted (Figure S3 in Supporting Information S1). As a reference slip rate distribution, we choose a model that balances low residual velocities with a low number of unique slip rate magnitudes.

Using the cumulative velocity field, we focus on the average slow slip rate that has taken place across the 44 cataloged events since 2007, rather than on individual event slip distributions (Figure 6b). We estimate slow slip rates up to 23 mm/year, with a region of >20 mm/year occurring beneath the Olympic Peninsula (46.8°–48.0°N, 30–40 km depth). Additional patches of faster slip (>12 mm/year) occur around latitudes 40°–41°N, 41.5°–42.5°N, and 44.3°–45.3°N. Along the subduction interface, we find a mean slow slip rate of 1.1 mm/year above 20 km depth and 6.4 mm/year below 20 km down to the bottom of the modeled interface at 50 km (with neither mean considering the enforced zero slip on triangles lining the updip or downdip edge). The cumulative moment rate below 20 km depth is 6.9 times that above 20 km, despite the total area of the deep interface being just 15% larger than the shallow interface. Slip rates in the strike-parallel direction are generally slower than those in the dip-slip direction, except beneath southern Vancouver Island (Figure S6 in Supporting Information S1). Residual velocities in this reference model average 0.68 mm/year (Figures S3 and S4b in Supporting Information S1).

3. Interseismic Coupling Models

3.1. Calculating Pure Interseismic Velocities

From the PANGA position time series, we remove estimated SSE displacements and steps due to nontectonic signals (offsets due to equipment maintenance and seasonal variation) and earthquakes (but not postseismic signatures [Michel et al., 2019]; Text S4 in Supporting Information S1) so that these corrected positions nominally reflect the contributions from crustal block motion and interseismic strain accumulation (blue points in Figure 2, top). By removing SSE displacements, we interpret the resultant velocities as influenced by subduction zone coupling that occurs between SSEs, which we term pure interseismic velocities. Retaining SSE displacements in the velocity field calculation would underestimate the pure interseismic velocities that reflect subduction zone strain accumulation. For each GPS station, positions from days occurring during a cataloged SSE were removed and all subsequent positions were adjusted using the associated estimated SSE displacements.

We use the cleaned, inter-SSE daily positions to calculate pure interseismic velocities as a ~14-year (2007–2021) average using a Median Interannual Difference Adjusted for Skewness (MIDAS) robust trend estimator (Blewitt et al., 2016). MIDAS calculates the slope for all pairs of position observations separated by 1 year. If a pair a year apart (±36 days [10%]) cannot be found, the algorithm moves on to the next day. To reduce bias, slopes that are more than two standard deviations away from the median are removed, so that the majority of data fit a normal distribution. The final velocity is the median of all slopes calculated for that station. Due to the assumption that calculated slopes fit a normal distribution, the uncertainty associated with each station's velocity is determined from the standard deviation of that normal distribution (Blewitt et al., 2016; Text S4 in Supporting Information S1). We combine these calculated velocities with a data set from McCaffrey et al. (2013) to place the PANGA observations from the Cascadia fore arc in a more regional GPS velocity field (Figure 1), rotating the PANGA field into the regional reference frame (Text S5 in Supporting Information S1). The uncertainties associated with the McCaffrey et al. (2013) data set were scaled to be similar in magnitude to the pure interseismic MIDAS uncertainties so that the two data sets had similar influence on the estimated block model parameters.

Net interseismic velocities (calculated without removing SSE displacements) show northeastward movement relative to stable North America, with the highest velocities near the coast and decreasing inland (Figures 1 and 4b), illustrating shortening in the direction of plate convergence. In contrast, pure interseismic velocities (Figure 4a) show similar northeastward velocities but are faster than net velocities by an average of ~2 mm/year and up to 6 mm/year (Figure 4c). These differences are most apparent above the 30–50 km subduction depth contours and specifically around Puget Sound, where many SSEs have been detected.

3.2. Interseismic Block Modeling

We use an elastic block model (Meade & Loveless, 2009) with embedded TVR optimization algorithm (Evans et al., 2015) to estimate the spatial distribution of slip deficit rate on the Cascadia subduction interface from the pure interseismic velocities. The elastic block model assumes that GPS velocities arise from interseismic slip deficit on block-bounding faults and crustal block motions (Meade & Loveless, 2009), and we find that even when slip deficit is confined to the shallow portion of the subduction interface (<30 km), far-field velocities can be reasonably well fit, albeit with some systematic north-directed residuals above the 30 km slab contour (Figure S9a in Supporting Information S1). Owing to the lack of GPS stations on the Juan de Fuca plate, we use an a priori Euler pole describing the rotation of the Juan de Fuca plate relative to North America to constrain its motion (DeMets et al., 2010). We estimate spatially variable slip deficit rate on the same network of TDEs used to model slow slip, imposing a constraint that slip deficit on the downdip edge of the subduction interface is zero. We define coupling as the ratio of slip deficit magnitude to plate convergence magnitude, with positive coupling where the dip-component of slip deficit is positive, consistent with strain accumulation.

As was the case with the estimated slow slip distributions, we varied λ, the strength of the regularization in the block model estimation framework, seeking results that were simple in their spatial distribution while still closely matching the GPS observations (Figures S1, S2, and S9 in Supporting Information S1). Models with a significant proportion of overcoupled (coupling >1, or slip deficit rate exceeding the plate convergence rate) elements were considered unlikely depictions of actual fault behavior as they imply that more than 100% of the relative plate motion goes into the strain accumulation process (Figures S1 and S2 in Supporting Information S1). The
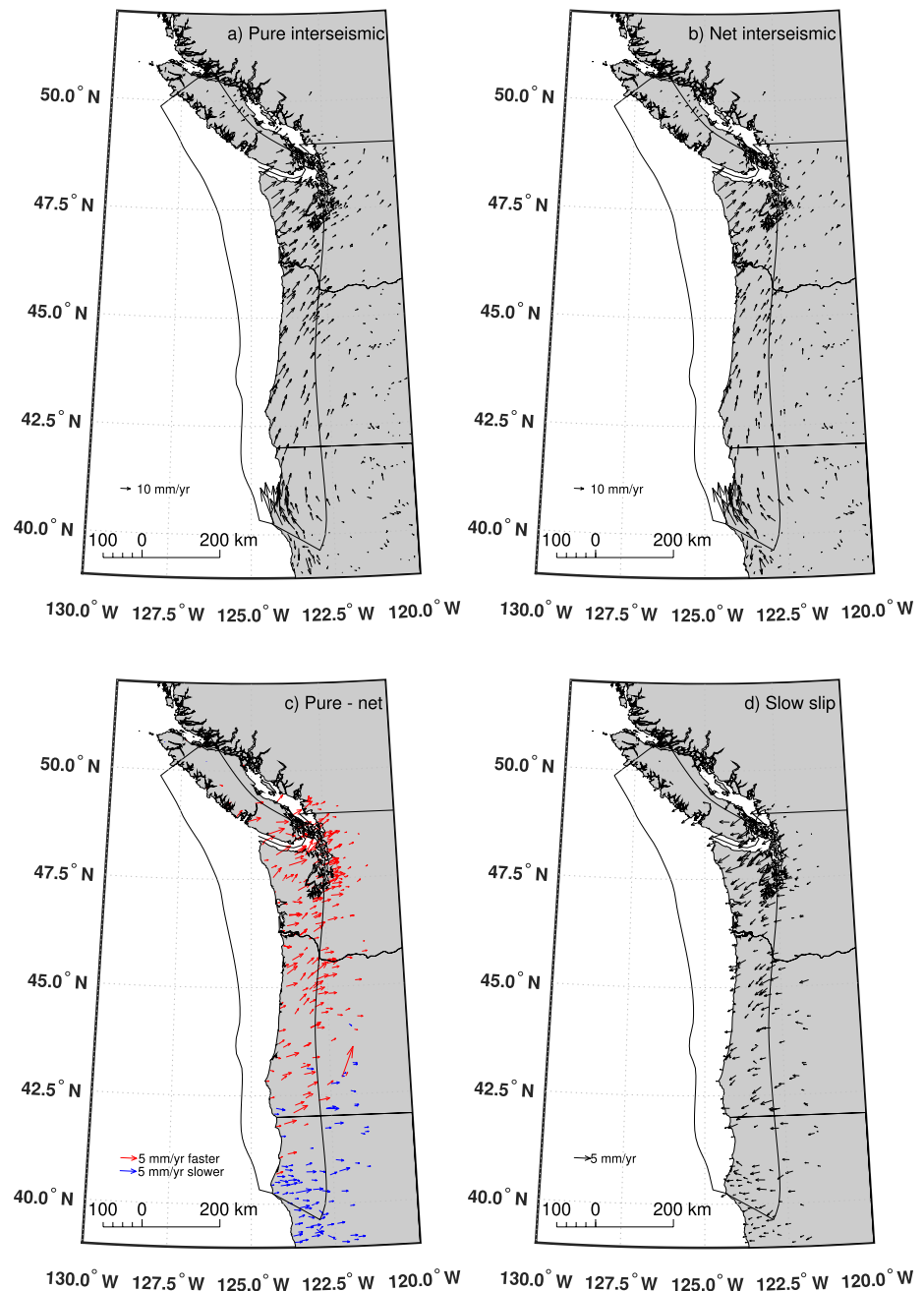
Figure 4. (a) Pure interseismic velocities, calculated from position time series corrected for slow slip event displacements, (b) net interseismic velocities, calculated from position time series that include effects of slow slip events, (c) difference between pure and net interseismic velocities, and (d) cumulative effects of slow slip events (SSE), represented as cumulative displacement divided by the 13-year time period considered here. All velocities are expressed relative to a nominal stable North American reference frame. In (a) and (b), the contribution to velocity from block rotation, as estimated in the pure interseismic block model, has been removed. In (c), red vectors indicate pure interseismic speeds faster than net interseismic speeds and blue vectors the pure interseismic speeds slower than net interseismic speeds. Velocities in (c) and (d) are nearly opposite, because we use slow slip displacements to correct net interseismic position time series (b) to yield pure interseismic velocities (a).

number of estimated overcoupled TDEs decreased with increasing GPS misfit and model simplicity, and we selected a model that balanced low GPS misfit with few overcoupled elements (Figure S1 in Supporting Information S1). Across stations in the greater Cascadia region (39°N–52°N, 120°W–130°W), residual speeds average
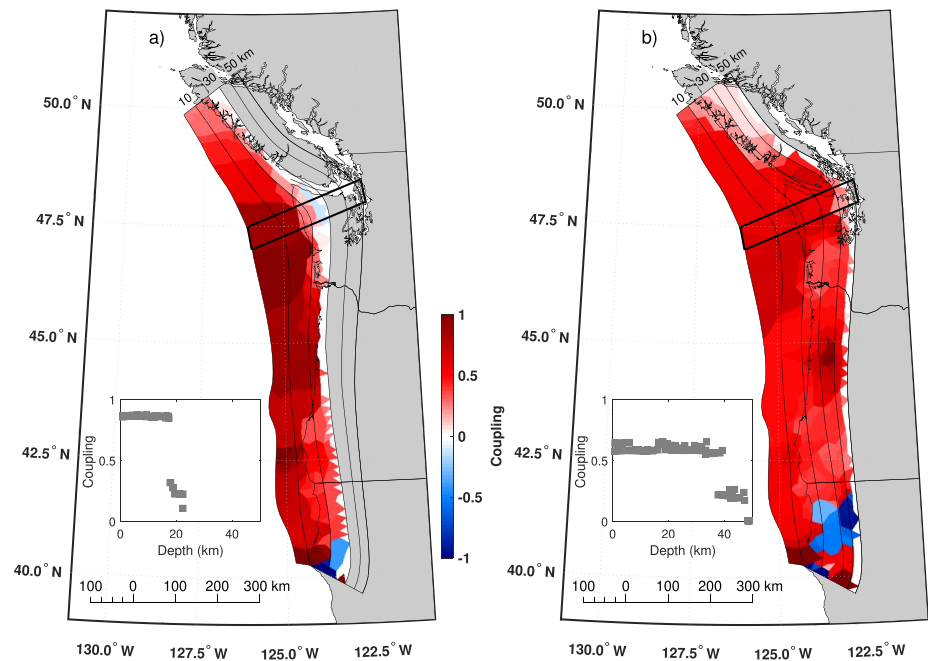
Figure 5. Cumulative coupling distribution made using (a) ~14 years (2007–2021) average net interseismic velocities, uncorrected for SSE displacements, allowing slip deficit to extend down to 30 km depth, but constraining slip deficit to be 0 at the downdip extent; (b) ~14 years average pure interseismic velocities, corrected for SSE displacements, allowing slip deficit to extend down to 50 km depth, but constraining slip deficit to be 0 at the downdip extent. We define coupling as the ratio of slip deficit magnitude to plate convergence magnitude, with positive coupling where the dip-component of slip deficit is positive. The inset shows the coupling fraction (≥0 shown) versus slab depth for elements that lie within the bold black rotated rectangle.

1.36 mm/year in the net interseismic model and 1.31 mm/year in the pure interseismic model (Figures S1, S2, and S9 in Supporting Information S1).

To test previous assumptions about the downdip extent of subduction zone coupling, we allow coupling to extend to a depth of 50 km in modeling pure interseismic GPS velocities. If coupling can extend to such depths while fitting the constraining velocities, deep slip deficit could explain the occurrence of SSEs. We also generated models constrained by net interseismic velocities, calculated by applying the MIDAS algorithm to position time series that still include SSE displacements. In these models, we used a representation of the subduction zone with a downdip extent of 30 km, consistent with previous assumptions of the downdip extent of the seismogenic zone (Schmalzle et al., 2014). The deeper extent of permitted coupling in the pure interseismic block models tests whether slip deficit at depths up to 50 km may be released by slow slip, while the net interseismic models reflect previous assumptions (Petersen et al., 2015; Schmalzle et al., 2014) that the deep occurrence of slow slip is itself an indicator that, at least averaged over decadal timescales, slip deficit does not accumulate below 30 km. The pure and net models should not necessarily be directly comparable, as we suggest that they reflect different sets of processes: the pure model isolates slip deficit accumulation, while the net model assumes that the impact of SSEs is already considered in the constraining velocity field.

3.3. Interseismic Coupling Distribution

Distinct spatial patterns in coupling are present in the pure and net interseismic models. In the net interseismic model, where the fault extends to 30 km depth, estimated strong coupling (slip deficit rate >0.8 of the relative plate motion rate) is restricted to offshore regions, with an abrupt decrease with depth, in part enforced by the assumption of zero coupling along the downdip edge of the modeled fault (Figure 5a). In the pure interseismic model, coupling is permitted to 50 km, and areas of estimated moderate coupling (slip deficit rate >0.6 of the relative plate motion rate) offshore of the Olympic Peninsula (47.5°N) extend to about 30–40 km depth (Figure 5b). In the pure interseismic model, the zone of estimated coupling <30 km is spatially consistent with previous
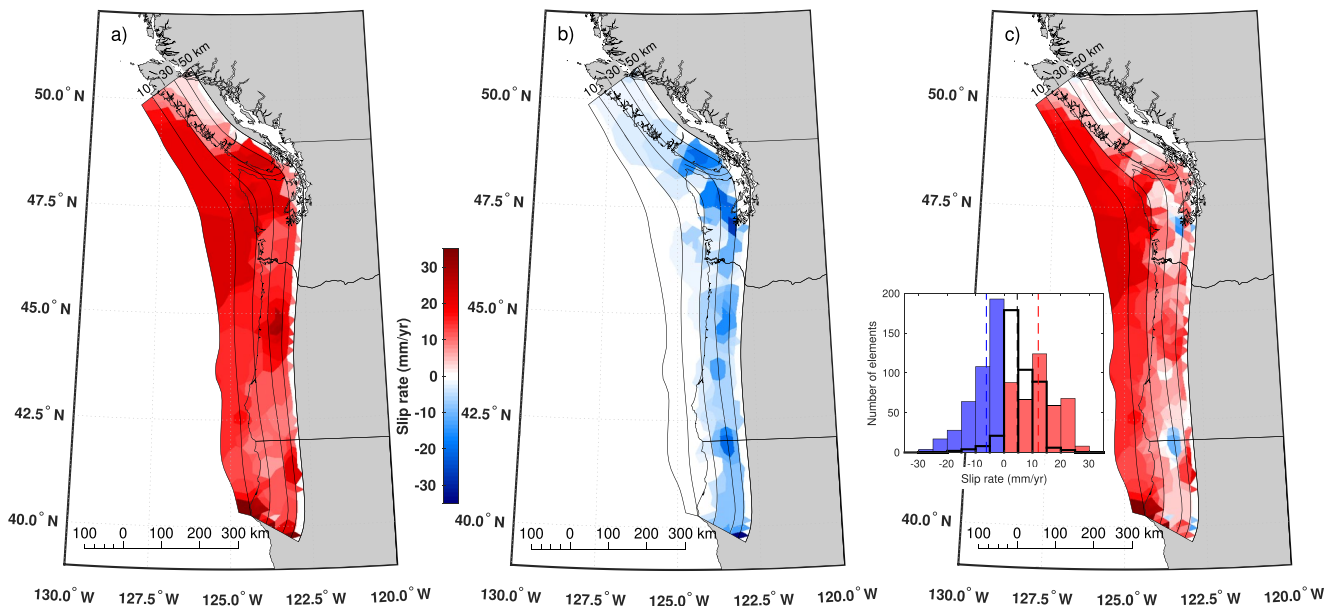
Figure 6. (a) Slip deficit rate distribution estimated using ~14 years (2007–2021) duration pure interseismic velocities on a slab interface extending to 50 km depth, but constraining slip deficit to be 0 at the downdip extent. (b) Estimated slip rate constrained by surface displacements from geodetically detected slow slip events, 2007–2021. (c) Summed slip deficit rates obtained by superimposing the slip deficit (a) and slow slip (b) rates. The inset shows frequency distributions (as bars) and median values (as dashed vertical lines) of slip deficit rates below 30 km depth (except those lining the downdip edge of the fault) for the cumulative inter-SSE slip deficit rates (in red), the cumulative slow slip rates (in blue), and the summed slip deficit rates (unfilled, bold black outlines).

estimates (Michel et al., 2019; Petersen et al., 2015; Schmalzle et al., 2014) though lower in magnitude, while the deeper zone is unique to the model using the 50 km geometry. In general, coupling decreases more gradually with depth than in the net interseismic model (Figure 5, insets).

While the downdip variation in coupling is notable, there are also variations along strike. In the net interseismic model, strong (>0.8) coupling extends from 43.5°N to 48°N, off the coast of the Olympic Peninsula and extending toward central Oregon. In the pure interseismic model, areas of shallow coupling are less intense and are more segmented with an area of slightly lower coupling at 47.5°N. The deeper areas of high coupling are further segmented along strike with one area under the Olympic Peninsula (48°N) and the other further south at 44°N.

The southern extreme of the subduction interface, bordering the east-west striking transform fault near the Mendocino Triple Junction, shows anomalous coupling values (Figure 5). We estimate coupling >1 and coupling <0 (reflecting thrust-sense slip faster than the plate convergence rate) on some elements in this region, perhaps resulting from complications arising from proximity to the triple junction and the associated fault interactions. Because these coupling values might arise from signals other than that of interseismic strain accumulation on the subduction interface, the southernmost triangular elements were not considered when determining which models were most feasible.

4. Discussion

4.1. Comparing Slip Processes on the Cascadia Subduction Zone

The spatial relationship between slow slip and coupling has implications for the accumulation of slip deficit at depth, and therefore the potential size of the seismogenic zone. Using the slip deficit rate extracted from the pure interseismic block models and the estimated slow slip rate, we can calculate the cumulative slip deficit rate over the ~14 years studied.

Expectedly, mapped pure interseismic slip deficit rate matches the pattern of coupling with a shallow zone of fast slip deficit located off the coast that extends beneath the Olympic Peninsula (Figures 5b and 6a). The deeper distribution of high slip deficit rate shows spatial coincidence with patterns seen in the cumulative slow slip (Figure 6) but is generally larger in magnitude (thin vs. thick solid black lines in Figure 7). These similarities in
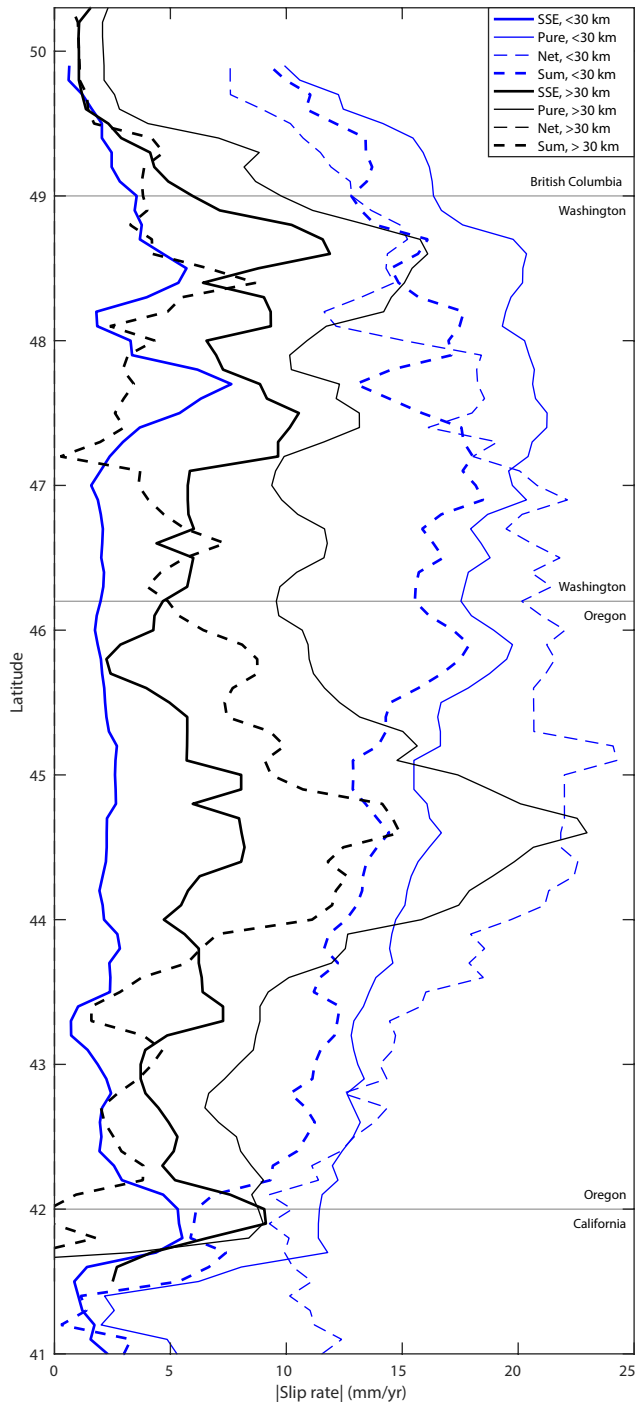
Figure 7. Along-latitude averages of pure interseismic slip deficit (a; Pure), cumulative slow slip rate (b; SSE), the sum of these distributions (c; Sum), and net interseismic slip deficit from a model allowing coupling down to 30 km (Net). We interpolated slip rates along 5 km depth intervals of the Cascadia Subduction Zone interface, then averaged the rates for all intervals shallower than 30 km (blue) and deeper than 30 km (black). The net interseismic slip deficit is exactly zero below 30 km depth because the modeled fault extended to 30 km.

deep slip deficit and cumulative slow slip suggest that SSEs release some of the estimated pure interseismic slip deficit at depth. We suggest that the two zones of pure interseismic strain accumulation are likely relieved by distinct slip processes: the shallow (0–30 km) seismogenic zone where slip deficit accumulates over the interseismic period hosts infrequent megathrust earthquakes and is largely unaffected by SSEs, and the deeper zone of coupling characterized by more frequent, periodic occurrence of SSEs.

When the slip rate from the SSEs is superimposed on the pure interseismic slip deficit distribution, the summed slip deficit speed at depth (>20 km) is reduced (Figures 6c and 7) and resembles more closely the slip deficit distribution resulting from the net interseismic model (Figures 5a and 7) and previous estimates of strain accumulation in Cascadia (Schmalzle et al., 2014). While there is extant slip deficit and slow slip, the median rate of the summed slip deficit on the deeper (>30 km) portion of the interface is 4.6 mm/year compared with a median of 5.4 mm/year of cumulative slow slip and 12.0 mm/year of pure interseismic slip deficit (inset, Figure 6c). In other words, since 2007, estimated slow slip has reduced the deep pure slip deficit by about 61%. This is comparable to previous suggestions that SSEs accommodate ~60% (Schmalzle et al., 2014; Schmidt & Gao, 2010) or ≥75% (Bartlow, 2020; Chapman & Melbourne, 2009) of the plate convergence rate. A block model using net interseismic velocities yet allowing coupling to 50 km depth shows a similar slip deficit distribution (Figure S11 in Supporting Information S1) to the summed slip deficit rate (Figure 6c) at depths below 30 km (Figure S12 in Supporting Information S1).

The slow slip and interseismic slip deficit distributions were estimated independently using different modeling frameworks (Sections 2.3 and 3.2). However, we use these different frameworks because each is most suitable for the respective constraining velocity field. Our method for detecting SSEs isolates reversals in the east position time series that we attribute to thrust-sense slip on the underlying subduction zone. We interpret the interseismic velocity fields to reflect not only elastic strain accumulation related to subduction zone slip processes but also tectonic plate motions (McCaffrey et al., 2013), and so we use a block model as a means of interpretation. In practice, the estimated tectonic plate motion contribution to the interseismic velocity fields is smaller than that from subduction interface slip processes (averaging 2.5 and 7.2 mm/year, respectively, across PANGA stations north of 41°N, away from substantial influence of Mendocino Triple Junction complexity). The estimated slip deficit and slow slip distributions are not exact mirrors of each other, yielding nonzero summed slip deficit (Figures 6c and 7). Simulations of great earthquakes in Cascadia (Frankel et al., 2018) assume a downdip limit of coseismic rupture at 30 km, based on locking contours from Petersen et al. (2015) and Frankel et al. (2015), while our models suggest that slip deficit may accumulate deeper as well. The remaining slip deficit downdip of 30 km depth after adding slow slip (Figures 6c and 7) raises the question of whether deep slip deficit could be released seismically, making larger the potential area that might rupture in a future seismic event.

4.2. The Kinematics and Mechanics of Deep Slip Deficit and Slow Slip

GPS stations in the fore arc can be used to infer subduction processes kinematically but do not give direct insights into frictional processes occurring on the subduction interface. Due to increases in temperature, frictional sliding is not thought to be able to occur >30 km depth in Cascadia (Hyndman &

Wang, 1993; Schmalzle et al., 2014; Wirth & Frankel, 2019), which would preclude the possible accumulation of deep slip deficit at such depths. However, the recurrence of SSEs indicates release of strain >30 km, which in turn suggests its accumulation.

Gao and Wang (2017) proposed a rheological explanation for slow slip at depth, suggesting that increased temperature below approximately 20 km depth (around the 400° isotherm) marks the downdip end of the seismogenic zone, and increased pore fluid pressure around 40 km depth could explain an isolated zone where frictional slip is favored over viscous flow, allowing periodic slow slip. Their results, which give insights into the mechanical behavior of the fault, are consistent with our kinematic findings, in that they show a shallow seismogenic zone and a deeper zone characterized by the periodic recurrence of SSEs. Here, we propose that interseismic strain accumulation is responsible for slow slip at depth, and therefore coupling extends deeper than previously suggested.

While Gao and Wang (2017) do not discuss the possibility of the zone of SSEs slipping coseismically during a megathrust rupture, they indicate that the zone must be at least mildly velocity weakening in order to support short-duration, periodic slow slip. According to their rheological models of Cascadia, separating the seismogenic zone and the zone of slow slip is a ~30-km-wide viscous gap that would serve to attenuate any interaction between the two frictional zones. Specifically, a SSE would not be able to rapidly apply stress to the seismogenic zone in order to trigger a megathrust earthquake. While coupling does not necessarily indicate frictional nature of the fault, we do not observe such a separation between the shallow and deep coupled zones, though we used total variational regularization (Sections 2.3 and 3.2) in an attempt to image sharp boundaries in slip distribution. The current station distribution has relatively high resolving power in imaging subduction zone slip around 20–40 km depth (Figure S7 in Supporting Information S1), but our presented models do not show a local minimum in coupling between the shallow and deep portions of the megathrust. The checkerboard test in Figure S7 in Supporting Information S1 shows 10–20-km-wide "haloes" of intermediate magnitude slip resolved between the zero and nonzero patches of the test slip distribution, indicating the wavelength of resolved slip signatures. This wavelength is similar to the width of the proposed viscous gap for northern Cascadia (Gao & Wang, 2017). Better resolution of the coupling distribution could provide information about potential triggering of megathrust earthquakes by SSEs, as has been documented on the southern Mexico subduction zone (Graham et al., 2014; Radiguet et al., 2016), where no viscous gap was modeled by Gao and Wang (2017).

4.3. Vertical Motion on the Olympic Peninsula

GPS data offer insights into the nature of fault coupling but have only been available in Cascadia since the mid-1990s, and a dense array of stations has been available for less time. Tide and leveling data span ~50–70 years (Alba et al., 2019; Burgette et al., 2009; Krogstad et al., 2016), giving a longer look at interseismic vertical motion in Cascadia, but they do not necessarily differentiate between periods of inter-SSE uplift and periods of slow slip. If vertical deformation observed from tide and leveling data matches predicted net interseismic deformation, it implies that pure interseismic slip deficit would need to be released by slow slip, or some combination of aseismic and seismic slip.

From the pure and net interseismic block models, and the cumulative slow slip distribution, we calculate predicted vertical motion in the Olympic Peninsula region (Figure 8) and compare the predictions with observed motion from a leveling transect along the north coast of the Olympic Peninsula (Figure 9). Pure interseismic slip deficit yields subsidence across much of the Olympic Peninsula, extending inland to approximately 123.5°W, with a peak of subsidence offshore, about 15 km above the fault interface (Figure 8a). Inland of 123.5°W, there is a peak of uplift along the west side of Puget Sound, with decreasing uplift eastward. This uplift pattern is inconsistent with leveling observations, which show maximum uplift along the west coast of the Olympic Peninsula that decreases inland, with no subsidence on land (Krogstad et al., 2016). In contrast, vertical deformation arising solely from slow slip is nearly opposite of that from pure interseismic slip deficit west of ~123°W, and subsidence farther inland (Figure 8b).

When the vertical deformation signature from slow slip is added to that from pure interseismic slip deficit, the subsidence on the western Olympic Peninsula is reduced in extent and magnitude (Figure 8c), and the boundary between subsidence and uplift shifts westward, so that nearly the entire Olympic Peninsula uplifts. Although more consistent with the observed vertical deformation than the individual slip process contributions, the pattern predicted by a net interseismic model (Figure 8d), in which coupling only extends to 30 km depth on the subduction
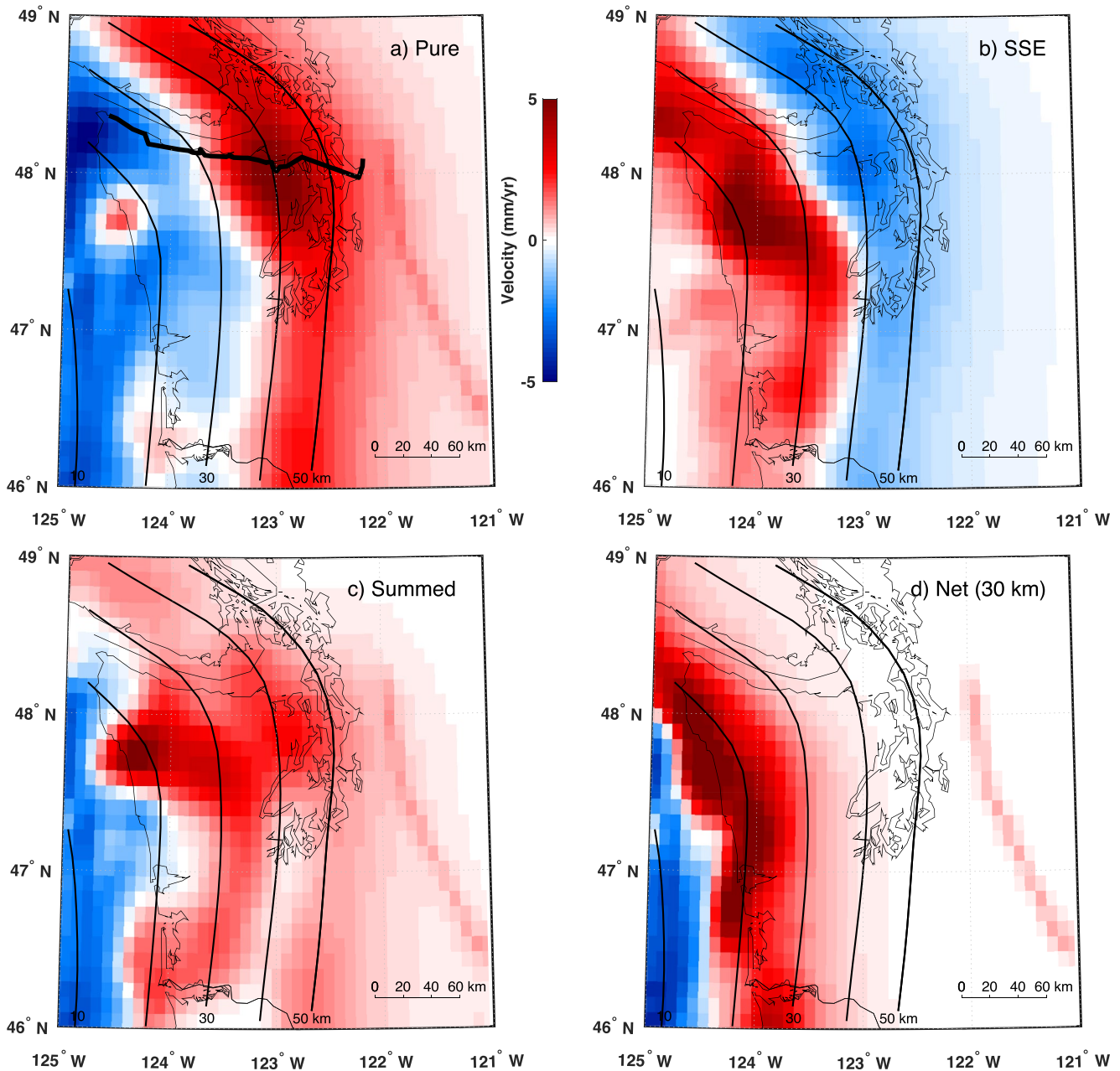
Figure 8. Modeled vertical velocity in the Olympic Peninsula region from (a) pure interseismic block model (Figure 7a), (b) slow slip events (SSE; Figure 7b), (c) sum of pure interseismic deformation and slow slip (i.e., sum of panels (a) and (b)), and (d) net interseismic block model (Figure 6a). Slab contours at 10 km intervals are shown as black lines. Bold black line around 48°N shows leveling profile presented in Krogstad et al. (2016), with data shown in Figure 9. The concentrated uplift east of 122ºW seen in the net, pure, and summed panels is related to slip on a crustal block boundary.

interface, more closely mimics the observations. This implies that, over the interseismic period, SSEs have a net effect on the vertical deformation of the overlying forearc. In other words, although inter-SSE interseismic slip deficit may extend to depths of 50 km to explain the presence of SSEs, over the ≥50-year time span captured by leveling data, deep slip deficit must be balanced by slip. Therefore, the aseismic slip rate may be variable during the interseismic period and our estimated 2007–2021 rate is slower than rates in the past and/or future decades.
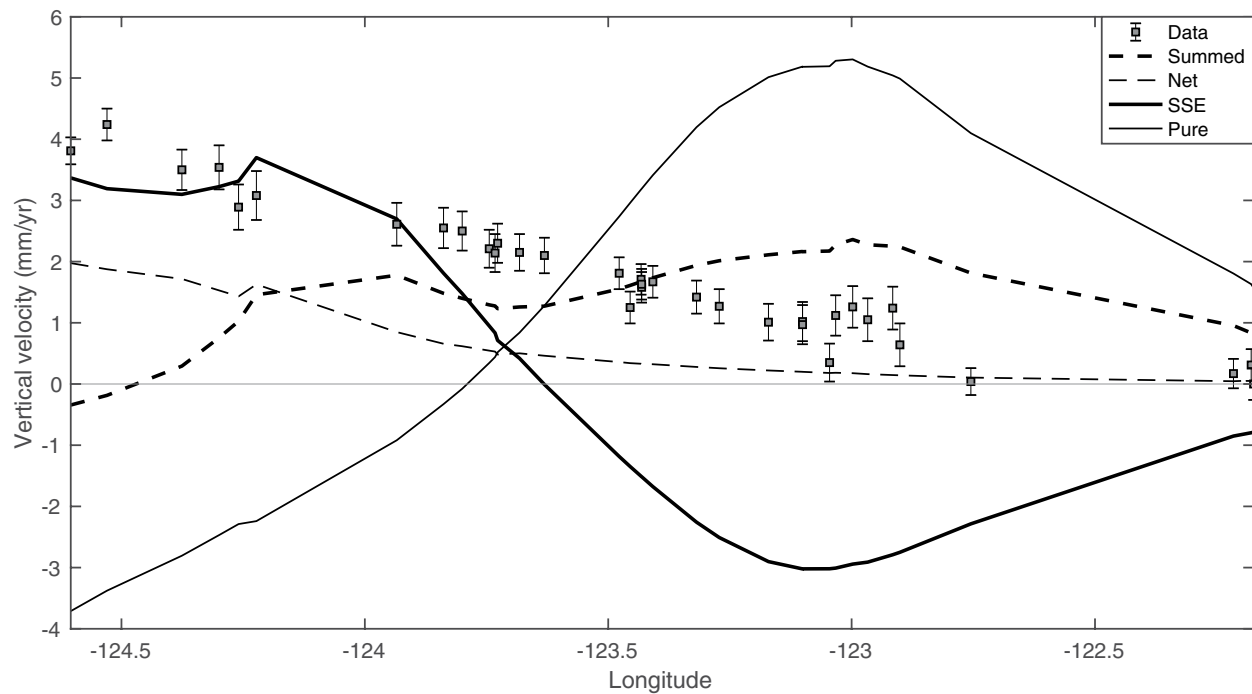
Figure 9. Observed and modeled vertical velocities along a leveling profile along the north coast of the Olympic Peninsula (bold black line in Figure 8a). Observed uplift rates decrease from west to east, similar to but faster than predicted uplift from the net interseismic model (Net). The summed contributions (Summed) of pure interseismic slip deficit (Pure) and slow slip (SSE) show slow subsidence on the far west side of the profile and steady uplift of ∼2 mm/year between −124.25° and −123° longitude before decreasing eastward.

5. Conclusions

Pure interseismic strain accumulation cannot be accurately represented in GPS time series that include reversals in motion from the recurrence of SSEs. Separating the effect of pure interseismic slip deficit from that of periodic slow slip occurrence allows for a more detailed analysis of slip processes on the subduction interface. Our pure interseismic block model shows a shallow zone of coupling consistent with previous estimates of the seismogenic zone, and a deeper zone of coupling that is characterized by the periodic recurrence of slow slip. These estimates extend coupling deeper than previous work in Cascadia and provide a potential explanation of the occurrence of slow slip at depth. However, the ability of SSEs to release all deep slip deficit is still an open question that greatly affects the potential seismic hazard of the region. While pure interseismic slip deficit at depth (>30 km) seems spatially correlated with slow slip, the rate of slip deficit is faster, with slow slip releasing about 61% of the estimated slip deficit over the 14-year period (2007–2021) studied here. Comparison of predicted vertical deformation on the Olympic Peninsula with leveling observations implies that slow slip must release all accumulated deep slip deficit at depth over longer timescales. Nonetheless, improved resolution of GPS inversions on the subduction interface is critical to understanding the relative spatial extents and magnitudes of both SSEs and coupling, which in turn is crucial to discerning the relative size and extent of the potential seismogenic zone in Cascadia.

Conflict of Interest

The authors declare no conflicts of interest relevant to this study.

Data Availability Statement

GPS time series data are available from the Pacific Northwest Geodetic Array (PANGA, http://www.panga. cwu.edu) and the tremor catalog is available from the Pacific Northwest Seismic Network (https://pnsn.org/ tremor). MATLAB functions for block modeling (https://doi.org/10.5281/ZENODO.4622191; Loveless, Meade, et al., 2021), slow slip event detection and velocity field estimation (https://doi.org/10.5281/ZENODO.4750416;

Loveless, Saux, et al., 2021), and slip estimation (https://doi.org/10.5281/ZENODO.4142503; Loveless & Evans, 2020) are freely available, and guidance about usage is listed in the Supporting Information S1.

References

Alba, S., Weldon, R. J., Livelybrooks, D., & Schmidt, D. A. (2019). Cascadia ETS events seen in tidal records (1980–2011). *Bulletin of the Seismological Society of America*, *109*(2), 812–821. https://doi.org/10.1785/0120180218

Almeida, R., Lindsey, E. O., Bradley, K., Hubbard, J., Mallick, R., & Hill, E. M. (2018). Can the updip limit of frictional locking on megathrusts Be detected geodetically? Quantifying the effect of stress shadows on near-trench coupling. *Geophysical Research Letters*, *45*, 4754–4763. https://doi.org/10.1029/2018GL077785

Atwater, B. F. (1987). Evidence for great Holocene earthquakes along the outer coast of Washington state. *Science*, *236*(4804), 942–944. https://doi.org/10.1126/science.236.4804.942

Bartlow, N. M. (2020). A long-term view of episodic tremor and slip in Cascadia. *Geophysical Research Letters*, *47*, e2019GL085303. https://doi.org/10.1029/2019GL085303

Blewitt, G., Kreemer, C., Hammond, W. C., & Gazeaux, J. (2016). MIDAS robust trend estimator for accurate GPS station velocities without step detection: MIDAS trend estimator for GPS velocities. *Journal of Geophysical Research: Solid Earth*, *121*, 2054–2068. https://doi.org/10.1002/2015JB012552

Brudzinski, M. R., & Allen, R. M. (2007). Segmentation in episodic tremor and slip all along Cascadia. *Geology*, *35*(10), 907. https://doi.org/10.1130/G23740A.1

Burgette, R. J., Weldon, R. J., & Schmidt, D. A. (2009). Interseismic uplift rates for western Oregon and along-strike variation in locking on the Cascadia Subduction Zone. *Journal of Geophysical Research*, *114*, B01408. https://doi.org/10.1029/2008JB005679

Bürgmann, R. (2018). The geophysics, geology and mechanics of slow fault slip. *Earth and Planetary Science Letters*, *495*, 112–134. https://doi.org/10.1016/j.epsl.2018.04.062

Chambolle, A. (2004). An algorithm for total variation minimization and applications. *Journal of Mathematical Imaging and Vision*, *20*, 89–97.

Chapman, J. S., & Melbourne, T. I. (2009). Future Cascadia megathrust rupture delineated by episodic tremor and slip. *Geophysical Research Letters*, *36*, L22301. https://doi.org/10.1029/2009GL040465

Crowell, B. W., Bock, Y., & Liu, Z. (2016). Single-station automated detection of transient deformation in GPS time series with the relative strength index: A case study of Cascadian slow slip. *Journal of Geophysical Research: Solid Earth*, *121*, 9077–9094. https://doi.org/10.1002/2016JB013542

DeMets, C., Gordon, R. G., & Argus, D. F. (2010). Geologically current plate motions. *Geophysical Journal International*, *181*(1), 1–80. https://doi.org/10.1111/j.1365-246X.2009.04491.x

Desbrun, M., Meyer, M., Schröder, P., & Barr, A. H. (1999). Implicit fairing of irregular meshes using diffusion and curvature flow. In *Proceedings of the 26th Annual Conference on Computer Graphics and Interactive Techniques*. New York: ACM Press/Addison-Wesley Publishing Co. https://doi.org/10.1145/311535.311576

Dragert, H., Wang, K., & James, T. S. (2001). A silent slip event on the deeper Cascadia subduction interface. *Science*, *292*(5521), 1525–1528. https://doi.org/10.1126/science.1060152

Dragert, H., Wang, K., & Rogers, G. (2004). Geodetic and seismic signatures of episodic tremor and slip in the northern Cascadia Subduction Zone. *Earth, Planets, and Space*, *56*(12), 1143–1150.

Evans, E. L., Loveless, J. P., & Meade, B. J. (2015). Total variation regularization of geodetically and geologically constrained block models for the Western United States. *Geophysical Journal International*, *202*(2), 713–727. https://doi.org/10.1093/gji/ggv164

Frankel, A., Chen, R., Peterson, M., Moschetti, M., & Sherrod, B. (2015). 2014 Update of the Pacific Northwest Portion of the U.S. National Seismic Hazard Maps. *Earthquake Spectra*, 31(8755-2930, 1944-8201), S131–S148. https://doi.org/10.1193/111314EQS193M

Frankel, A., Wirth, E., Marafi, N., Vidale, J., & Stephenson, W. (2018). Broadband synthetic seismograms for magnitude 9 earthquakes on the Cascadia megathrust based on 3D simulations and stochastic synthetics, Part 1: Methodology and overall results. *Bulletin of the Seismological Society of America*, *108*(5A), 2347–2369. https://doi.org/10.1785/0120180034

Gao, X., & Wang, K. (2017). Rheological separation of the megathrust seismogenic zone and episodic tremor and slip. *Nature*, *543*(7645), 416–419. https://doi.org/10.1038/nature21389

Goldfinger, C., Nelson, C. H., & Johnson, J. E. (2003). Holocene earthquake records from the Cascadia Subduction Zone and northern San Andreas Fault based on precise dating of offshore turbidites. *Annual Review of Earth and Planetary Sciences*, *31*, 555–577. https://doi.org/10.1146/annurev.earth.31.100901.141246

Graham, S. E., DeMets, C., Cabral-Cano, E., Kostoglodov, V., Walpersdorf, A., Cotte, N., et al. (2014). GPS constraints on the 2011–2012 Oaxaca slow slip event that preceded the 2012 March 20 Ometepec earthquake, southern Mexico. *Geophysical Journal International*, *197*(3), 1593–1607. https://doi.org/10.1093/gji/ggu019

Grant, M., & Boyd, S. (2008). Graph implementations for nonsmooth convex programs. In V. Blondel, S. Boyd, & H. Kimura (Eds.), *Recent advances in learning and control* (pp. 95–110). Berlin, Germany: Springer-Verlag Limited.

Grant, M., & Boyd, S. (2014). *CVX: Matlab software for disciplined convex programming, version 2.1*. Retrieved from http://cvxr.com/cvx

Harris, R. A., & Segall, P. (1987). Detection of a locked zone at depth on the Parkfield, California, segment of the San Andreas fault. *Journal of Geophysical Research*, *92*(B8), 7945–7962.

Herman, M. W., Furlong, K. P., & Govers, R. (2018). The accumulation of slip deficit in subduction zones in the absence of mechanical coupling: Implications for the behavior of megathrust earthquakes. *Journal of Geophysical Research: Solid Earth*, *123*, 8260–8278. https://doi.org/10.1029/2018JB016336

Holtkamp, S., & Brudzinski, M. R. (2010). Determination of slow slip episodes and strain accumulation along the Cascadia margin. *Journal of Geophysical Research*, *115*, B00A17. https://doi.org/10.1029/2008JB006058

Hyndman, R. D., & Wang, K. (1993). Thermal constraints on the zone of major thrust earthquake failure: The Cascadia Subduction Zone. *Journal of Geophysical Research*, *98*(B2), 2039–2060. https://doi.org/10.1029/92JB02279

Krogstad, R. D., Schmidt, D. A., Weldon, R. J., & Burgette, R. J. (2016). Constraints on accumulated strain near the ETS zone along Cascadia. *Earth and Planetary Science Letters*, *439*, 109–116. https://doi.org/10.1016/j.epsl.2016.01.033

Li, S., Wang, K., Wang, Y., Jiang, Y., & Dosso, S. E. (2018). Geodetically inferred locking state of the Cascadia megathrust based on a viscoelastic Earth model. *Journal of Geophysical Research: Solid Earth*, *123*, 8056–8072. https://doi.org/10.1029/2018JB015620

Loveless, J. P., & Evans, E. L. (2020). *triinv: Inversion of displacement and stress data using triangular dislocation elements in Matlab (Version v1.0)*. Zenodo. https://doi.org/10.5281/ZENODO.4142503

Loveless, J. P., & Meade, B. J. (2011). Spatial correlation of interseismic coupling and coseismic rupture extent of the 2011 MW = 9.0 Tohoku-oki earthquake. *Geophysical Research Letters*, *38*, L17306. https://doi.org/10.1029/2011GL048561

Loveless, J. P., Meade, B. J., & Evans, E. L. (2021). *Blocks: Analysis of plate boundary deformation using geodetic data (Version v1.0)*. Zenodo. https://doi.org/10.5281/ZENODO.4622191

Loveless, J. P., Saux, J. P., & Molitors Bergman, E. G. (2021). *posarrays: Matlab utilities for reading and analyzing GPS position data (Version 1.0)*. Zenodo. https://doi.org/10.5281/ZENODO.4750416

McCaffrey, R., King, R. W., Payne, S. J., & Lancaster, M. (2013). Active tectonics of northwestern U.S. inferred from GPS-derived surface velocities. *Journal of Geophysical Research: Solid Earth*, *118*, 709–723. https://doi.org/10.1029/2012JB009473

McCrory, P. A., Blair, J. L., Oppenheimer, D. H., & Walter, S. R. (2006). *Depth to the Juan de Fuca slab beneath the Cascadia subduction margin: A 3-D model for sorting earthquakes. Data Series*. Reston, VA: U.S. Geological Survey.

Meade, B. J. (2007). Algorithms for the calculation of exact displacements, strains, and stresses for triangular dislocation elements in a uniform elastic half space. *Computers & Geosciences*, *33*(8), 1064–1075. https://doi.org/10.1016/j.cageo.2006.12.003

Meade, B. J., & Loveless, J. P. (2009). Block modeling with connected fault-network geometries and a linear elastic coupling estimator in spherical coordinates. *Bulletin of the Seismological Society of America*, *99*(6), 3124–3139. https://doi.org/10.1785/0120090088

Michel, S., Gualandi, A., & Avouac, J.-P. (2019). Interseismic coupling and slow slip events on the Cascadia megathrust. *Pure and Applied Geophysics*, *176*, 3867–3891. https://doi.org/10.1007/s00024-018-1991-x

Miller, M. M., Melbourne, T., Johnson, D. J., & Sumner, W. Q. (2002). Periodic slow earthquakes from the Cascadia Subduction Zone. *Science*, *295*(5564), 2423. https://doi.org/10.1126/science.1071193

Moreno, M., Rosenau, M., & Oncken, O. (2010). 2010 Maule earthquake slip correlates with pre-seismic locking of Andean subduction zone. *Nature*, *467*, 198–202. https://doi.org/10.1038/nature09349

Nishimura, T., Matsuzawa, T., & Obara, K. (2013). Detection of short-term slow slip events along the Nankai Trough, southwest Japan, using GNSS data. *Journal of Geophysical Research*, *118*, 3112–3125. https://doi.org/10.1002/jgrb.50222

Oleskevich, D. A., Hyndman, R. D., & Wang, K. (1999). The updip and downdip limits to great subduction earthquakes: Thermal and structural models of Cascadia, south Alaska, SW Japan, and Chile. *Journal of Geophysical Research: Solid Earth*, *104*(B7), 14965–14991. https://doi.org/10.1029/1999JB900060

Petersen, M. D., Moschetti, M. P., Powers, P. M., Mueller, C. S., Haller, K. M., Frankel, A. D., et al. (2015). The 2014 United States National Seismic Hazard Model. *Earthquake Spectra*, *31*(S1), S1–S30. https://doi.org/10.1193/120814EQS210M

Pollitz, F. F., & Evans, E. L. (2017). Implications of the earthquake cycle for inferring fault locking on the Cascadia megathrust. *Geophysical Journal International*, *209*(1), 167–185. https://doi.org/10.1093/gji/ggx009

Protti, M., Gonzalez, V., Newman, A. V., Dixon, T. H., Schwartz, S. Y., Marshall, J. S., et al. (2014). Nicoya earthquake rupture anticipated by geodetic measurement of the locked plate interface. *Nature Geoscience*, *7*(2), 117–121. https://doi.org/10.1038/ngeo2038

Radiguet, M., Cotton, F., Vergnolle, M., Campillo, M., Walpersdorf, A., Cotte, N., & Kostoglodov, V. (2012). Slow slip events and strain accumulation in the Guerrero gap, Mexico. *Journal of Geophysical Research*, *117*, B04305. https://doi.org/10.1029/2011JB008801

Radiguet, M., Perfettini, H., Cotte, N., Gualandi, A., Valette, B., Kostoglodov, V., et al. (2016). Triggering of the 2014 Mw 7.3 Papanoa earthquake by a slow slip event in Guerrero, Mexico. *Nature Geoscience*, *9*, 829. https://doi.org/10.1038/ngeo2817

Rousset, B., Bürgmann, R., & Campillo, M. (2019). Slow slip events in the roots of the San Andreas fault. *Science Advances*, *5*(2), eaav3274. https://doi.org/10.1126/sciadv.aav3274

Rudin, L. I., Osher, S., & Fatemi, E. (1992). Nonlinear total variation based noise removal algorithms. *Physica D: Nonlinear Phenomena*, *60*(1–4), 259–268. https://doi.org/10.1016/0167-2789(92)90242-F

Schmalzle, G. M., McCaffrey, R., & Creager, K. C. (2014). Central Cascadia Subduction Zone creep. *Geochemistry, Geophysics, Geosystems*, *15*, 1515–1532. https://doi.org/10.1002/2013GC005172

Schmidt, D. A., & Gao, H. (2010). Source parameters and time-dependent slip distributions of slow slip events on the Cascadia Subduction Zone from 1998 to 2008. *Journal of Geophysical Research*, *115*, B00A18. https://doi.org/10.1029/2008JB006045

Szeliga, W., Melbourne, T., Santillan, M., & Miller, M. (2008). GPS constraints on 34 slow slip events within the Cascadia Subduction Zone, 1997–2005. *Journal of Geophysical Research: Solid Earth*, *113*, B04404. https://doi.org/10.1029/2007JB004948

Wang, K., & Tréhu, A. M. (2016). Invited review paper: Some outstanding issues in the study of great megathrust earthquakes—The Cascadia example. *Journal of Geodynamics*, *98*, 1–18. https://doi.org/10.1016/j.jog.2016.03.010

Wech, A. G., Creager, K. C., & Melbourne, T. I. (2009). Seismic and geodetic constraints on Cascadia slow slip. *Journal of Geophysical Research*, *114*, B10316. https://doi.org/10.1029/2008JB006090

Wirth, E. A., & Frankel, A. D. (2019). Impact of down-dip rupture limit and high-stress drop subevents on coseismic land-level change during Cascadia megathrust earthquakes. *Bulletin of the Seismological Society of America*, *109*(6), 2187–2197. https://doi.org/10.1785/0120190043

References From the Supporting Information

Geuzaine, C., & Remacle, J.-F. (2009). Gmsh: A 3-D finite element mesh generator with built-in pre- and post-processing facilities. *International Journal for Numerical Methods in Engineering*, *79*(11), 1309–1331. https://doi.org/10.1002/nme.2579

Loveless, J. P., & Meade, B. J. (2010). Geodetic imaging of plate motions, slip rates, and partitioning of deformation in Japan. *Journal of Geophysical Research*, *115*, B02410. https://doi.org/10.1029/2008JB006248

Meade, B. J., & Loveless, J. P. (2017). Block motion changes in Japan triggered by the 2011 great Tohoku earthquake. *Geochemistry, Geophysics, Geosystems*, *18*, 2459–2466. https://doi.org/10.1002/2017GC006983